

# Near Infrared Chromosphere Observatory

Barry J. LaBonte<sup>a</sup>, David M. Rust<sup>a</sup>, Pietro N. Bernasconi<sup>a</sup>, Manolis K. Georgoulis<sup>a</sup>,  
Nicola J. Fox<sup>a</sup>, Wolfgang Kalkofen<sup>b</sup>, Haosheng Lin<sup>c</sup>

<sup>a</sup>Johns Hopkins University Applied Physics Laboratory

<sup>b</sup>Smithsonian Astrophysical Observatory

<sup>c</sup>Institute For Astronomy, University of Hawaii

## ABSTRACT

NICO, the Near Infrared Chromosphere Observatory, is a platform for determining the magnetic structure and sources of heating for the solar chromosphere. NICO, a balloon-borne observatory, will use the largest solar telescope flying to map the magnetic fields, velocities, and heating events of the chromosphere and photosphere in detail. NICO will introduce new technologies to solar flight missions, such as wavefront sensing for monitoring telescope alignment, real-time correlation tracking and high-speed image motion compensation, and wide aperture Fabry-Perot etalons for extended spectral scanning.

**Keywords:** solar chromosphere, solar magnetic fields, high resolution imaging

## 1. SCIENCE GOALS

The solar magnetic field controls the structure, energy flow, mass balance, and eruptive/explosive activity of the solar atmosphere. The science goals for NICO focus on the role of the magnetic field in the solar chromosphere. This part of the atmosphere has received relatively less attention, but its importance is being more generally recognized.

### 1. Chromospheric heating

Recent solar space missions, including Yohkoh, the Solar and Heliospheric Observatory (SOHO), and the Transition Region and Coronal Explorer (TRACE), focus on the difficult problem of coronal heating. The flux needed to heat the quiet corona is  $10^{5.5}$  erg/cm<sup>2</sup>/sec. The problem of heating the chromosphere is even more difficult. The flux needed to maintain the quiet chromosphere is  $10^{6.4}$  erg/cm<sup>2</sup>/sec – nearly 10 times as much as the corona. The lifetime of a typical chromospheric structure is only  $10^2$  to  $10^3$  sec, whereas the lifetime of typical coronal loops is  $10^3$  to  $10^5$  sec. The problem, then, is that much more power and many more energizing events are needed to maintain the solar chromosphere than the corona. Since the energy budget of the chromosphere is so much higher than that of the corona and since all coronal magnetic fields link to the chromosphere, we must understand the chromosphere in order to understand the corona.

Coronal and chromospheric heating are intimately coupled<sup>1</sup>. Coronal heating literally cannot occur in a vacuum. Without active heating of the chromosphere, the supply of mass to the corona is too small to balance losses to the solar wind and settling in cooling loops. The corona would evacuate and disappear. Chromospheric heating is thought to be powered by waves, either MHD or acoustic modes<sup>2,3</sup>, or by magnetic reconnection<sup>4</sup>. Combination of both mechanisms is also possible<sup>5</sup>. NICO has the spatial and temporal resolution to detect relevant wave modes and reconnection events and to establish their relationship to chromospheric thermal conditions. Observations in a set of spectral lines (Table 1) that cover a range of altitudes in the solar photosphere and chromosphere establish the vertical structure of the magnetic field and propagation of mass flows.

**Table 1. NICO spectral lines and broadband blocking filters.**

Spectral line [Å]	H $\alpha$ 6563	HeI 10830	CaII 8498	CaII 8542	CaII 8662	FeI 8688	KI 7699
Landé $g_{\text{eff}}$	1.05	1.2	1.07	1.2	0.8	1.66	1.33
Height [km]	2000 $\pm$ 500	2000 $\pm$ 500	1100 $\pm$ 400	1000 $\pm$ 500	1000 $\pm$ 500	500 $\pm$ 100	450
Blocker bandpass [Å]	20	30	20	20	30	10	10

## 2. The magnetic transition region

Energy dissipation in the corona may be due to reconnections of magnetic fields evolving to achieve a state of minimum energy. Dissipation in a quasi-steady regime can heat the static corona; dissipation in a catastrophic regime can drive coronal mass ejections (CME), accelerate energetic particles, heat thermal flare plasma, and power MHD shocks. Precise knowledge of the vector magnetic fields in the photosphere and chromosphere is crucial for probing this energy release process. Absent direct measurements of coronal magnetic fields, estimates of coronal magnetic fields are usually made by extrapolation<sup>6,7</sup>, using the magnetic field on the photosphere as a boundary condition. There are major issues of physical conditions in the solar chromosphere<sup>8,9</sup> that must be resolved before we can have confidence in the extrapolations.

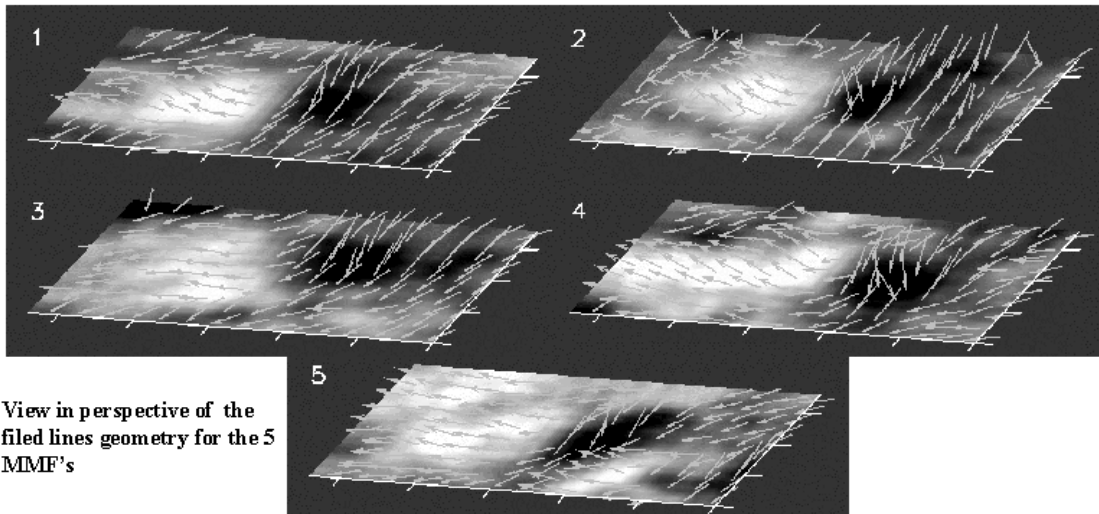
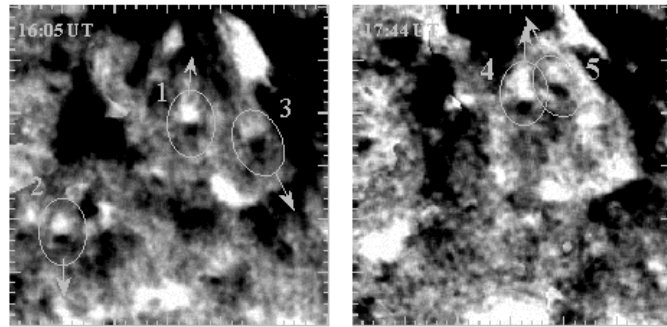
In particular, there is an important boundary layer in the chromosphere: the *magnetic transition region* (MTR), in which the plasma  $\beta$  (ratio of thermal energy density to magnetic energy density) drops dramatically. In the photosphere, the high gas density and low filling factor of the magnetic field ensures that  $\beta > 1$ . At the top of the chromosphere, the magnetic field expands to fill the volume, and the decreased density brings down the value to  $\beta < 1$ . The MTR is the layer in which the magnetic fields tend to become force-free. NICO observes the complete Stokes vector spectra in lines formed over a wide range of altitudes. Interpretation of the Stokes spectra enables understanding the magnetic field vector throughout the photosphere and chromosphere. Accurate characterization of the nonmagnetic forces and their decay with altitude permit field extrapolation from a valid boundary surface.

Figure 1 shows an example of the importance of stable time series at high spatial resolution to deciphering the true structure of the solar magnetic field. These FGE images<sup>10</sup> revealed a new class of dipolar moving magnetic features (MMF). As the lower panels show, these dipoles are U-loops, stitched into the photosphere from an overlying horizontal field, rather than  $\Omega$ -loops emerging from the solar interior.

### Magnetic structure of MMF's

Longitudinal magnetograms on the left indicate location and direction (arrows) of the 5 selected MMF's.

Tick marks separation is 1".



View in perspective of the field lines geometry for the 5 MMF's

Figure 1. FGE discovery of a class of dipolar magnetic structures that are U-loops, stitched into the solar photosphere from an overlying horizontal field.

NICO's field-of-view (FOV) encompasses an entire solar active region, ensuring that the connectivity of the fields is correctly determined. Because the ratio of Zeeman splitting to Doppler broadening increases with wavelength, we are driven to the near infrared rather than the extreme ultraviolet (EUV). NICO's wavelength range includes the spectrum lines that have the highest combinations of chromospheric opacity and magnetic sensitivity.

### 3. What processes provide the mass in the chromosphere?

The corona is filled with material that is often close to hydrostatic equilibrium. The high coronal temperature ( $> 1$  MK) sets a large pressure scale height; the long cooling time permits material to remain in the corona for extended periods. Chromospheric structure is not close to hydrostatic equilibrium. The vertical extent of spicules, fibrils, cool loops, and filaments far exceeds the pressure scale height at chromospheric temperatures. The gravitational potential energy content of the magnetized chromosphere structure thus far exceeds the thermal energy content. The failure of hydrostatic equilibrium in the chromosphere is a profound physical problem. The relative difficulty of heating the chromosphere as opposed to the corona is dwarfed by the relative difficulty of supplying momentum to the chromosphere. No such requirement exists for the corona. NICO spatial and temporal resolution, achieved over a range of altitudes, permit the measurement of the physical conditions that loft and support cool material. The wide FOV includes entire filaments. It enables the observation of conditions at both ends of magnetic field lines simultaneously, important for assessing the role of various physical processes such as siphon flows.

### 4. NICO relation to other programs

The Long Duration Balloon (LDB) platform is ideal for NICO science. Ground-based observations offer limited spatial and temporal coverage at high spatial resolution, despite improvements in telescope performance and site selection. The limiting photometric resolution is set by seeing, even with the use of adaptive optics, and varies rapidly with space and time over a useful field-of-view (FOV)<sup>11</sup>. Space-based observations, such as those anticipated from Solar-B, permit instrument-limited data quality. However, the available data are resource limited. Downlink bandwidth limits the total spatial and temporal coverage. Instrument complexity limits the range of altitudes that are measured. NICO complements space instruments with higher peak datarates, broad altitude coverage, and shorter time to launch. The LDB platform also offers a low cost access to space quality conditions for the development of instrument technology and data analysis tools.

**Table 2. Summary of NICO mission and payload characteristics.**

Mission Information	
Vehicle:	LDB Zero-Pressure Balloon 2.7 Mm <sup>2</sup> volume
Launch location:	Williams Field, Antarctica; 77.9 deg S, 167.1 deg E, at sea level
Baseline launch	December 15 - January 15; 1 month launch window
Launch options:	Every Antarctic summer from December to January
Mission duration:	10 - 20 days
Flight trajectory:	Circumpolar, at 73 - 82 deg S latitude
Flight altitude:	37 km $\pm$ 2 km; 30 km minimum altitude
Telemetry:	Primary: TDRSS satellite relay; continuous 4 kb/sec up- & downlink Backup: INMARSAT-C sat.relay; packets of max 256 bits per 50 min up- & downlink
Ground station:	Primary: Williams Field, Antarctica Secondary: NSBF operation control center, Palestine Texas
Payload Characteristics	
Mass:	1600 kg
Dimensions:	5.6 x 1.5 x 5.5 m (W x D x H)
Attitude:	Gravity-gradient; reference system Sun; $\pm$ 10" RMS pointing accuracy
Power:	Solar cells; max power production 1300 Watts
Instrument:	80 cm diam. Cassegrain telescope; alt-azimuth mount Imaging Vector Magnetograph
Data Storage:	On-board; 20 x 160 GB hard drives; total = 3200 GB

## 2. IMPLEMENTATION

### 5. Mission summary

NICO is a proposed new approach for determining the magnetic structure and sources of energy and mass for the solar chromosphere. A balloon-borne observatory will use the largest solar telescope flying and very high data rates (Table 2) to map the magnetic fields, velocities, and heating events of the chromosphere and photosphere in unprecedented detail. NICO (Figure 2) is based on the Flare Genesis Experiment (FGE), which has pioneered in the application of technologies important to NASA's flight program. NICO will also introduce new technologies, such as wavefront sensing for monitoring telescope alignment; real-time correlation tracking and high-speed image motion compensation for smear-free imaging; and wide aperture Fabry-Perot filters for extended spectral scanning.

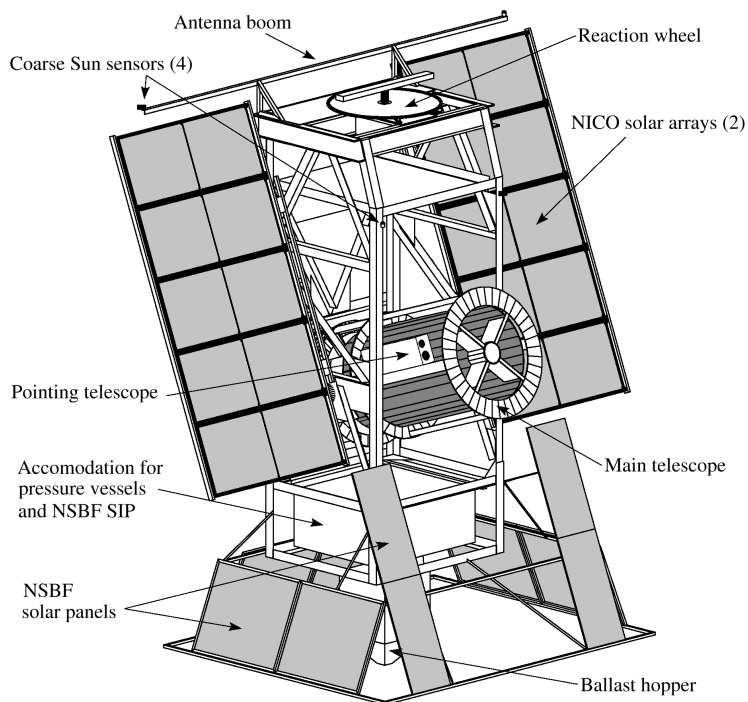


Figure 2. Schematic of the NICO payload configuration. Computer systems reside in the pressure vessel mounted to the ballooncraft. Ground telemetry provides for realtime commanding and quicklook data downlink. After initial solar acquisition via coarse Sun sensors, the pointing telescope provides error signals to drive the main telescope elevation drive and azimuth reaction wheel to maintain solar pointing.

### 6. Telescope and instrument

The telescope is a classic Cassegrain design with an 80-cm diameter F/1.5 primary mirror made of Ultra-Low-Expansion glass. The secondary is made of single-crystal silicon, which provides excellent thermal conduction from the mirror surface to its mount, with negligible thermal distortion. The telescope structure is graphite-epoxy for lightweight and high thermal stability. A third mirror acts as a heat dump. It passes the light from a 15-mm diameter aperture in its center, corresponding to a 322"-diameter circle on the solar surface, while the rest of the solar radiation is reflected back out of the front of the telescope.

The telescope supplies the selected segment of the solar image to a polarization and spectral analysis package as shown in Figure 3. The polarimeter optics are placed in a collimated beam that precedes all oblique reflections. The spectrometer, cameras, and auxiliary optics are folded into a pressure vessel that remains at 1 atmosphere pressure. Table 3 summarizes the NICO instrument characteristics.

**Table 3. Instrument characteristics**

Major System	Optical Parameters				
<b>Cassegrain Telescope</b>	Primary:	80 cm Diameter; F/1.5; ULE			
	Secondary:	10 cm Diameter, silicon			
	Primary focus:	322" Diameter field stop; F/12			
	Focal plane:	F/37; 200" x 200" field of view; 0.097" per pixel			
	Diffraction limit:	$\lambda$ [Å]	6563	8500	11000
Resolution		0.21"	0.27"	0.35"	
<b>Spectral filter</b>	8 Positions filter wheel with 7 prefilter blockers with 10-30 Å bandpass				
	Dual Fabry-Pérot étalon:				
	WL range:	6500 - 11000 Å			
	FSR:	26.4 - 74.1 Å			
	Bandpass:	0.08 - 0.224 Å			
<b>Polarimeter</b>	2 Liquid crystal variable retarders + 1 linear polarizer				
	2 Calibration filter wheels with polarizers and $\lambda/4$ retarders				
	Records Stokes $I, Q, U, V$ in 4 seconds with 4 consecutive exposures				
<b>Science Camera</b>	Thomson Camelia 4M				
	2K x 2K pixels; 12 bit; 14 $\mu$ m square pixels; 4.2 images/sec				
<b>IMC</b>	Algorithm:	Correlation tracking			
	Optics:	Secondary mirror on hexapod act. with 6 deg. of freedom			
		90/10 beam splitter; refocusing lenses			
Detector:	256" x 256" pix camera; 0.2"/pix; 100 frames/sec				
<b>Autonomous Telescope Alignment</b>	Algorithm:	Curvature wavefront sensing			
	Optics:	Secondary mirror on hexapod act. with 6 deg. of freedom			
		Movable beam folding mirror + 2 beam splitters (66/33, 50/50)			
	Detectors:	3 Cameras; 256" x 256" pixels; 0.2"/pix			
Simultaneously record 3 images at focus, focus $\pm$ 5 mm					

A pair of liquid crystal retarders produces polarization modulation. FGE demonstrated that the liquid crystal retarders work fine in the balloon environment (air pressure 4-mB, temperature 20° C). The full Stokes vector ( $I, Q, U, V$ ) is measured, using the 4-phase (mixed states) modulation scheme implemented in the Mees Solar Observatory Imaging Vector Magnetograph<sup>12</sup>. The modulation package consists of two variable retarders with retardances  $\delta_1$  and  $\delta_2$  respectively, and fast axes at fixed angles 90° and 45°, followed by a linear polarizer at 0°. The resultant intensity signal  $S$  is:

$$S = 1/2 ( I + Q \cos \delta_2 + U \sin \delta_1 \sin \delta_2 + V \cos \delta_1 \sin \delta_2 ).$$

To determine the full Stokes vector [ $I, Q, U, V$ ] is necessary record a series of images with the retarders at different setting. By choosing the retardance settings for the four measurements  $S_1, S_2, S_3,$  and  $S_4$  as follows:

$$\delta_1 = \{ \pi + \alpha, \pi + \alpha, \pi - \alpha, 2\pi - \alpha \},$$

$$\delta_2 = \{ \pi - \beta, \pi + \beta, 2\pi - \beta, 2\pi - \beta \},$$

where  $\alpha = \pi/4$ , and  $\beta = \arctan(\sqrt{2})$ , the full Stokes vector can then be calculated. The retardance is optimized for each wavelength.

Calibration optics are inserted upstream of the modulators at intervals to verify their performance in flight.

They consist of a set of linear polarizers at  $0^\circ$ ,  $45^\circ$ ,  $90^\circ$ ,  $135^\circ$  orientation angles followed by a series of  $\lambda/4$  retarders tuned for the observed wavelengths. These optical elements will be inserted in the optical path to produce various reference polarized beam states.

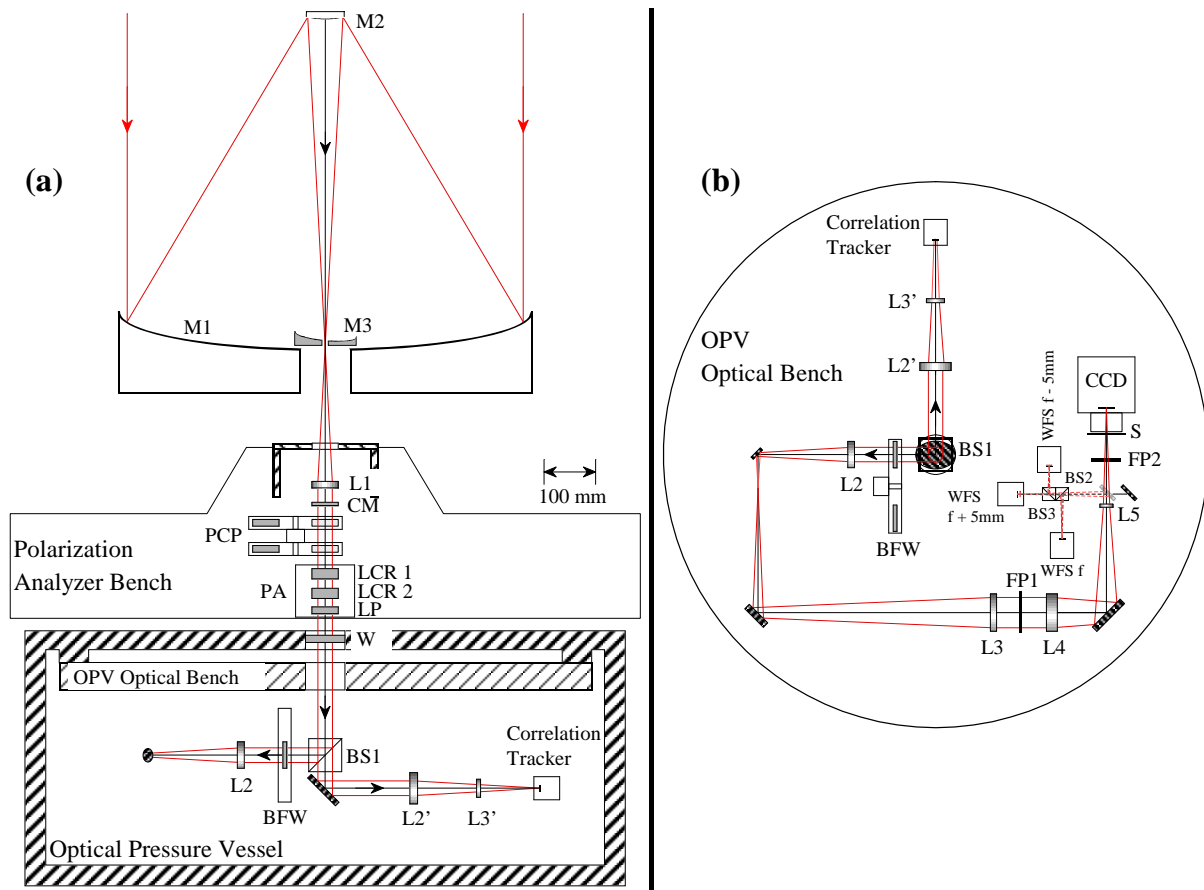


Figure 3. Optical layout of the NICO solar telescope and instrument. (a) Telescope optics and polarization analyzer + calibration unit. (b) View of the optics inside the OPV. M1 = primary mirror (ULE); M2 = secondary mirror (silicon); M3 = heat dump mirror; L1 = collimating lens; PCP = polarization calibration package; PA = polarization analyzer; LCR1-2 = liquid crystal retarders; LP = linear polarizer; W = OPV entrance window; BS1 = beam splitter (90/10); L2-5 and L2'-L3' = reimaging lenses; BFW = blockers filter wheel; FP1-2 = Fabry-Pérot étalons; S = camera shutter; BS2 = beam splitter (66/33); BS3 = beam splitter (50/50); WFS = wavefront sensing cameras in focus (f), at focus -5 mm (f-5mm), and at focus + 5 mm (f+5mm).

The spectrometer is a pair of Fabry-Perot etalons. The etalons are made from lithium niobate, and are electrically tuned in wavelength to scan the spectrum line selected by an order-sorting filter. The passband of a lithium-niobate étalon can be tuned through  $\sim 3\text{\AA}$  by varying the voltage between  $-3000$  and  $+3000$  V. To avoid the hazard of arcing at the 4-mB float pressure we installed the filters in a 1-atm pressurized vessel. Lithium-niobate étalons are sensitive to temperature changes, but they can be stabilized to  $5\text{-m\AA}$  by controlling their temperature with an accuracy of  $0.1^\circ\text{C}$ . For FGE, we implemented such a control system. We also monitored the temperature to  $0.01^\circ\text{C}$  and adjusted the drive voltage to further correct for the temperature effect.

The two Fabry-Pérot filters will be tuned synchronously so that two transmission peaks will always overlap. FP1 is in a collimated beam at an image of the entrance pupil, and it acts as the narrow-band wavelength selector. FP2 is just in front of the CCD camera in an F/37 converging beam. It has a broader bandpass and its function is mainly to block the adjacent transmission peaks from FP1 and pass only the target wavelength. Table 4 describes the parameters of the spectrometer, with: D the clear aperture of the

etalon; FSR the Free Spectral Range, i.e., the spectral distance between two peaks in the filter transmission;  $\Delta\lambda$  the bandpass (Full Width at Half Maximum, FWHM) of a single intensity peak; and F the finesse of the etalon, defined as:  $FSR/\Delta\lambda$ . The wide physical separation of the etalons eases the elimination of coherent reflections between etalons.

**Table 4. Spectral characteristics of the dual lithium niobate tunable Fabry-Pérot filter**

	FP1: D = 10 cm, F = 30		FP2: D = 6 cm, F = 16		Combined
$\lambda$ [Å]	$\Delta\lambda$ [Å]	FSR [Å]	$\Delta\lambda$ [Å]	FSR [Å]	FSR [Å]
6560	0.080	2.40	0.206	3.30	26.40
8500	0.134	4.02	0.346	5.53	44.23
10000	0.186	5.57	0.479	7.66	61.30
11000	0.224	6.74	0.579	9.27	74.15

The camera is a conventional CCD, operating at an image cadence  $\sim 1$  filtergram/sec. No other single detector covers the required wavelength range. The CCD image scale is arranged to provide diffraction-limited images, with a resolution of 0.2 to 0.3" depending on wavelength. On-board data storage is 3.2 Terabytes, adequate for continuous operations over the expected LDB duration. Typical observing sequences comprise spectropolarimetry in a set of lines, with the line choices, numbers of spectral positions, and image cadence chosen for the particular science objective. A baseline program of line and continuum images to record photospheric and chromospheric structure runs continuously through the mission.

### 7. Expected measurement precision

In the wavelength range 650–860 nm, NICO will acquire 2 images/sec, summed to give a signal-to-shot noise of 600 per 0.1" pixel. In the wavelength range 1000–1100 nm, NICO will acquire 1 image/sec with a signal-to-shotnoise of 250 per 0.1" pixel. The signal to noise can be improved by applying  $2 \times 2$  pixel binning to the images recorded above 1000-nm. At these wavelengths the telescope diffraction limit is 0.31" and  $2 \times 2$  pixels have a projected size of 0.194".

The expected velocity sensitivity is of order 5–10m/sec per observation. With 3 images/min, this is 3–6 m/sec/min -- not far from MDI. The actual error will be set by systematic errors including shutter jitter and étalon wavelength jitter/drift. The expected magnetic precision is of order 5 – 10 G for longitudinal flux density in the chromosphere. In the photosphere, the precision is 3 – 5 times better. The precision of transverse fields is 5 – 10 times worse. Averaging over space and/or time, or synchronous detection of periodic waves will improve precision. Accuracy of the field measures will be set by systematic errors in the interpretation of Stokes spectra into magnetic field vectors.

### 8. Image stability and quality

Two auxiliary light paths provide critical signals to achieve diffraction-limited spatial resolution. One path feeds a high-speed camera that records continuum images. Cross-correlation of the images measures residual image motion. The error signal drives a high-speed tip-tilt motion of the secondary. The balloon gondola is isolated from the balloon by an angular momentum transfer unit, shown in Figure 4. Windshake of the balloon gondola is measured and controlled through servo motions of the telescope mount to a level of order 10", as shown in Figure 5. The image motion compensation reduces the image motion to 0.1".

The second auxiliary path feeds a set of cameras that measure the wavefront errors of the imaging beam, using the method of wavefront curvature<sup>13,14,15</sup>. All compact large aperture telescopes designed for space flight have a fast focal ratio primary mirror. To achieve diffraction limited image quality, tolerances on alignment of the telescope optics are very tight. Launch and thermal stresses make it difficult to hold the alignment to tolerance. Inflight measurement of the wavefront errors permits active, low bandwidth correction of misalignment<sup>16</sup>. The NICO secondary mirror is articulated on a hexapod to correct misalignment.

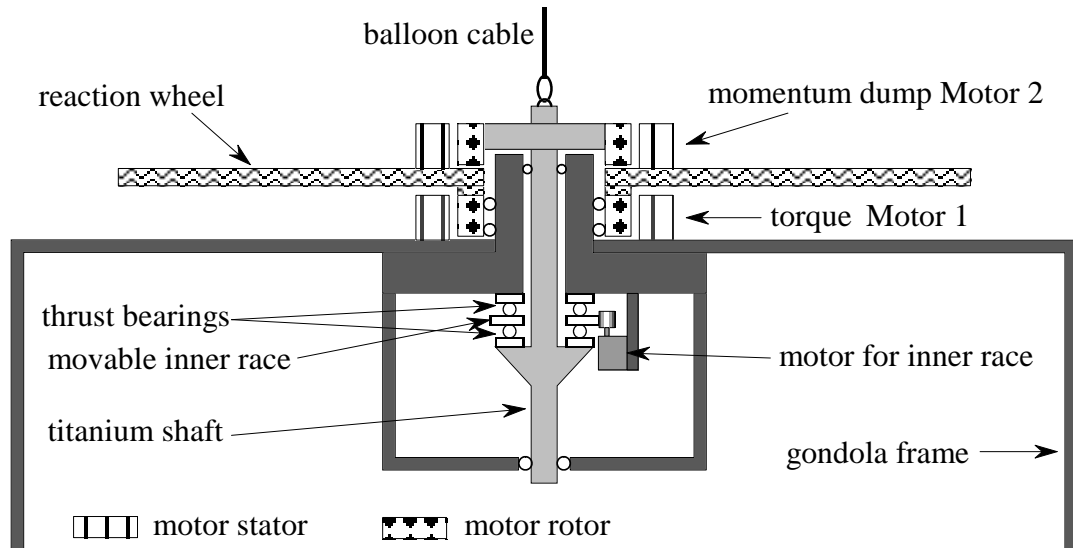


Figure 4. Cross-section Schematic of the NICO Momentum-Transfer-Unit.

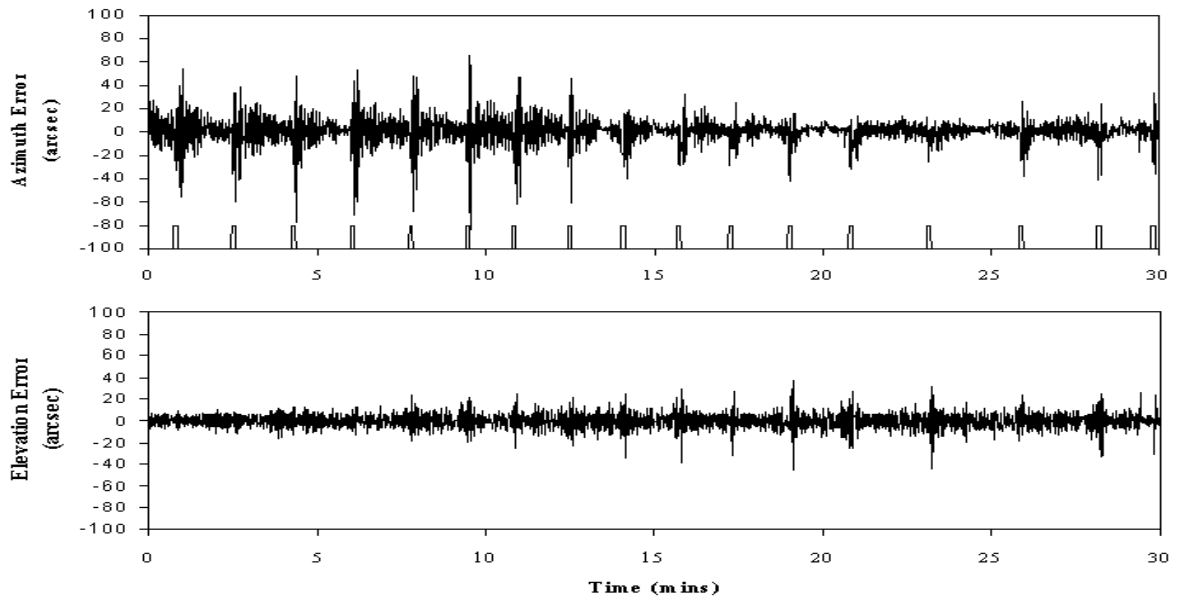


Figure 5. Telescope pointing errors during the January 2000 flight of FGE. RMS jitter was 8" in elevation and 13" in azimuth. Ticks at the bottom of the azimuth chart indicate periods of momentum transfer from the reaction-wheel to the balloon.

### 9. Command and data handling

Figure 6 shows a block diagram of the NICO command and data handling system. The control computers and data storage are sealed in a pressure vessel at 1 atmosphere, eliminating the need for costly vacuum-rated systems. Rapid improvements in compute speed and storage density since the flight of the FGE have direct benefit to NICO. They enable the more complex image quality systems and the higher datarate. Onboard storage capacity is 3.2 TB (uncompressed), compared to 80 GB for FGE, for example. Dedicated processors are used for the data-intensive tasks: the correlation tracker for image motion compensation; and

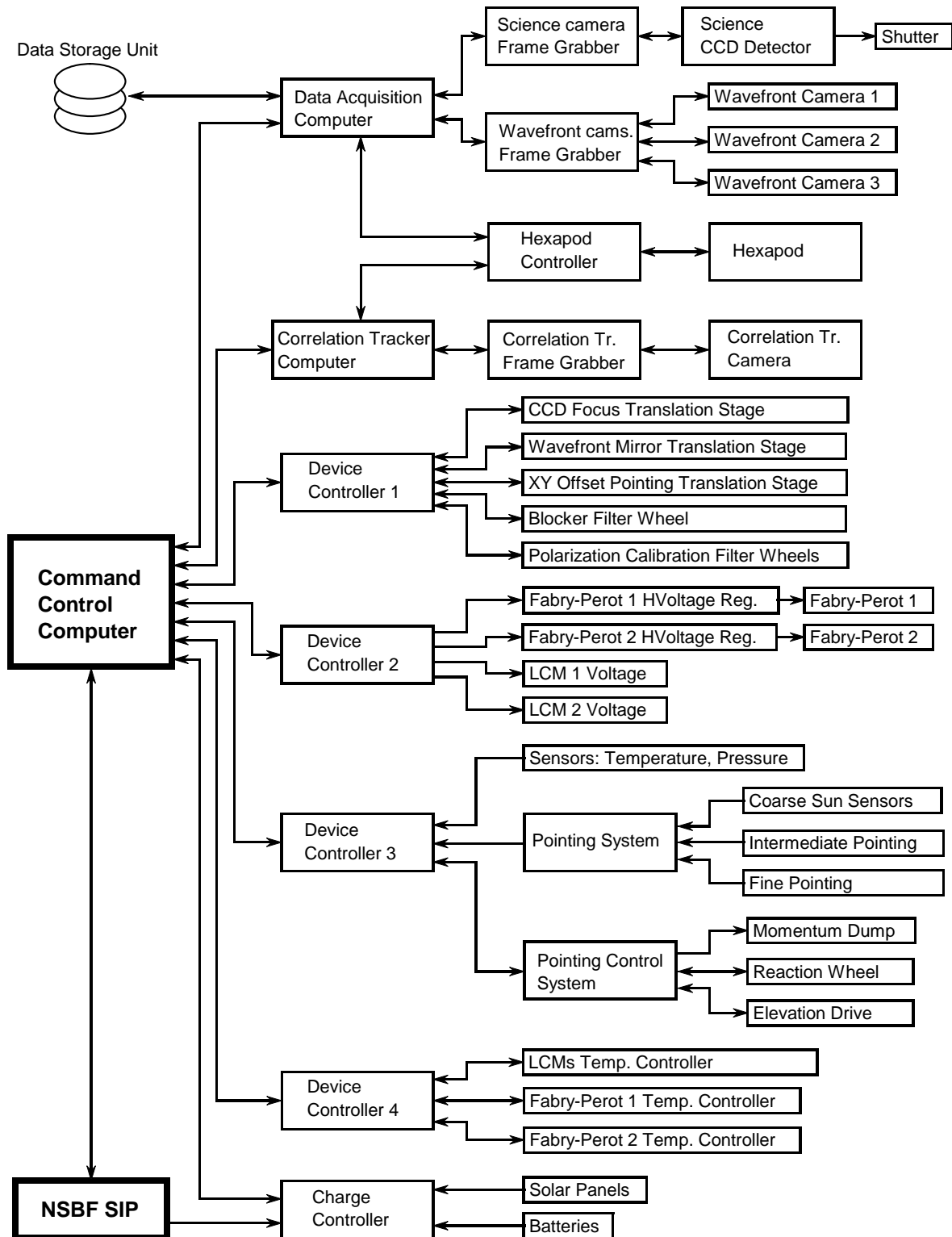


Figure 6. Block diagram of the NICO command and data handling system.

the data acquisition system. The latter processor also handles the wavefront analysis data during the brief intervals that system is used, since science data is not recorded during those times. Compared to FGE,

NICO has consequent improvements in spatial and temporal resolution and in completeness in probing the solar conditions over a range of altitude.

### 3. SUMMARY

Increasing attention in the science community to the need to measure the physical conditions in the solar chromosphere, particularly the magnetic field vector, emphasizes the value of the NICO science program. NICO provides coordinated data to enhance the scientific productivity of orbital solar missions. NICO uses the cost effective LDB platform to develop new hardware and software technologies.

### 4. REFERENCES

1. J. C. Brown, S. Krucker, M. Gudel, and A. O. Benz, "Mechanisms for dynamic coronal mass supply via evaporative solar micro-events", *Astron. Astrophys.* V. 359, pp. 1185-1194, 2000.
2. B. W. Lites, R. J. Rutten, and W. Kalkofen, "Dynamics of the solar chromosphere. I – Long-period network oscillations", *Astrophys. J.*, V. 414, pp. 345-356, 1993.
3. R. Kupke, B. J. LaBonte, and D. L. Mickey, "Observational study of sunspot oscillations in Stokes I, Q, U, and V", *Solar Phys.*, V. 191, pp. 97-128, 2000.
4. M. J. Aschwanden, C. J. Schrijver, and D. Alexander, "Modeling of coronal EUV loops observed with TRACE. I. Hydrostatic solutions with nonuniform heating", *Astrophys. J.*, V. 550, pp. 1036-1050, 2001.
5. A. Takeuchi and K. Shibata, "Magnetic reconnection induced by convective intensification of solar photospheric magnetic fields", *Astrophys. J.*, V. 546, pp. L73-L76, 2001.
6. C. E. Alissandrakis, "On the computation of constant alpha force-free magnetic field", *Astron. Astrophys.*, V. 100, pp. 197-200, 1981.
7. B. C. Low, "Magnetic field configurations associated with polarity intrusion in a solar active region. I – The force-free fields", *Solar Phys.*, V. 77, pp. 43-61, 1982.
8. T. R. Metcalf, L. Jiao, A. N. McClymont, R. C. Canfield, and H. Uitenbroek, "Is the solar chromosphere magnetic field force-free?", *Astrophys. J.*, V. 439, pp. 474-481, 1995.
9. M. K., Georgoulis, D. M. Rust, and P. N. Bernasconi, "On the force-freeness of photospheric magnetic fields in solar active regions: the current density method", *Astrophys. J.*, submitted, 2002.
10. P. N. Bernasconi, D. M. Rust, M.K. Georgoulis, and B. J. LaBonte, "Moving dipolar features in an emerging flux region", *Solar Phys.*, in press, 2002.
11. D. E. Potter, L. M. Close, F. Roddier, C. Roddier, J. E. Graves, M. Northcott, "A high resolution polarimetry map of the circumbinary disk around UY Aurigae". *Astrophys. J.*, V. 540, pp. 422-428, 2000.
12. D. L. Mickey, R. C. Canfield, B. J. LaBonte, K. D. Leka, M. F. Waterson, and H. M. Weber, "The Imaging Vector Magnetograph at Haleakala", *Solar Phys.*, V. 168, pp. 229-250, 1996.
13. R. Kupke, R. J. Roddier, and D. L. Mickey, "Curvature-based wavefront sensor for use on extended patterns", *Proc SPIE* V. 2201, Adaptive Optics in Astronomy, eds. M. A. Ealey and F. Merkle, pp. 519-527, 1994.
14. R. Kupke, R. J. Roddier, and D. L. Mickey, "Wavefront curvature sensing on extended arbitrary scenes: simulation results", *Proc SPIE* V. 3353, Adaptive Optical System Technologies, eds. D. Bonaccini and R. K. Tyson, p. 918, 1998.
15. G. Molodij, F. J. Roddier, R. Kupke, and D. L. Mickey, "Curvature wavefront sensor for solar adaptive optics", *Solar Phys.*, V. 206, pp. 189-207, 2002.
16. N. A. Roddier, D. R. Blanco, L. W. Goble, C. A. Roddier, "WIYN telescope active optics system", *Proc. SPIE* V.2479, Telescope Control Systems, ed. P. T. Wallace, pp.364-376, 1995.